Science Advances | AAAS

Manuscript Template

1
2
3
4 *Science Advances*
5 **Manuscript Template**
6
7
8
9 **General Instructions on using this template and submitting a new manuscript**
10 **to *Science Advances***
11
12
13 Use this template to speed the processing of your paper.
14
15
16 We need to accurately record
17 the title, authors, abstract, and other component parts of your paper so we can
18 enrich it with reference links and an accurate layout.
19
20
21 Please use the actual template starting on the next page, which
22 includes more specific formatting instructions.
23
24
25 You can submit your paper at https://cts.sciencemag.org
26
27
28 Additional instructions are available at
29 https://advances.sciencemag.org/content/information-authors
30
31
32 **When you are ready to submit, please delete this box**
33 **with all its contents.**
34 **Your manuscript should start on Page 1.**
35
36

-Bruker Confidential-

FRONT MATTER

3D photothermal AFM-IR tomography at nanometer scale

Alexandre Dazzi[1*], Jeremie Mathurin[1], Philippe Leclere[2], Pierre Nickmilder[2], Peter De Wolf[3], Martin Wagner[3], Qichi Hu[3], Ariane Deniset-Besseau[1]

Affiliations

[1] Institut de chimie Physique, Université Paris-Saclay – CNRS, 91400 Orsay, France
[2] Université de Mons
[3] Bruker Nano Surfaces, CA-93117 Santa Barbara, USA

[*]Corresponding author. Email alexandre.dazzi@universite-paris-saclay.fr

Abstract

Photothermal AFM-IR microscopy enables label-free chemical imaging with nanometer scale spatial resolution through the integration of atomic force microscopy (AFM) and infrared radiation. The capability for subsurface and 3D tomographic material analysis remains however largely unexplored. Here, we establish a simple and robust relationship between probing depth and laser repetition rate. Using this relationship, we demonstrate how Photothermal AFM-IR of thin surface/subsurface layers of PS-PMMA blends can result in 3D representations revealing the size and thickness of PS droplets in the PMMA matrix with nanometer scale resolution. Experimental findings are confirmed by analytical models.

Introduction

Atomic force microscopy (AFM) is an efficient technique for surface and sub-surface analysis at the nanometer scale, with applications in many scientific domains, including surface science, polymer science, cellular biology, molecular biology, molecular engineering, solid state physics, and medicine. The main advantages of this technique are its simplicity, robustness and the possibility to probe a wide variety of physical properties of the surface directly below the tip of the AFM with nanometer scale spatial resolution. Several AFM techniques have been developed to identify or discriminate the different nature or composition of materials through characterization of the chemical properties at the nanometer scale. During the last decades, two different approaches have been developed to perform unambiguous chemical characterization of samples using infrared spectroscopy: AFM-IR and s-SNOM. These AFM-based techniques allow one to measure the infrared spectra and chemical maps with a few nanometers of lateral resolution (*1*, *2*). Both techniques have advantages and drawbacks and can complement each other dependent on the type or nature of the sample to be studied.

Most AFM based techniques are probing the top surface of the sample. A few methods, such as scanning microwave impedance microscopy (SMIM), Kelvin probe force microscopy (KPFM), acoustic force microscopy and contact-resonance atomic force microscopy have shown a contrast imaging change related to different probing depths (*3*–*9*). The probing depth of SMIM is directly linked to the exponentially decreasing intensity of the microwave electric field from the surface into the sample. This effect is called skin effect and determines the probing depth and sampling volume of the measurement at a fixed frequency of analysis. The relationship between microwave frequency and probing depth can lead to sample investigation over various depths and enables one to reconstruct the real shape of buried structures similar to X-ray tomography (*10*). For acoustic

-Bruker Confidential-

87 force microscopy the dependency of the probing depth is more complex to determine as the physical
88 process involved is generated by nonlinear interaction between two acoustic waves. Both the
89 acoustic wave frequency and the frequency difference variation result in strong contrast variations
90 pointing to probing depth variations (*11*). As the AFM-IR technique is based on photothermal
91 excitation, the physics involved should be the same as for conventional photothermal spectroscopy
92 and the laser repetition rate used for infrared analysis should control the probing depth of each
93 measurement.
94 In this work, we present a full characterization of the probing depth for all commonly used AFM-IR
95 modes: resonance enhanced AFM-IR mode, tapping AFM-IR mode, and surface sensitive AFM-IR
96 mode (*12*) and propose a methodology to calibrate rigorously this property independently of the
97 type of cantilever used. Thanks to this knowledge, we show, how a 3D tomogram can be
98 reconstructed to visualize the full shape of polymer samples inside a matrix of another polymer,
99 based on data acquired in resonance enhanced AFM-IR mode.
100
101
102
103 **Results**
104
105 **Methodology and sample calibration for probing depth estimation**
106
107 The probing depth is mainly defined as a property that represents the depth sensitivity of a
108 surface characterization method. In the case of the AFM-IR technique, it means the ability to probe
109 the sample absorbance below its surface. In classical photothermal techniques, the probing depth is
110 associated with the thermal diffusion length L_{diff} which is dependent on the frequency (f) of the heat
111 modulation (*13*) :

112 $$L_{diff} \propto \frac{1}{\sqrt{f}} \qquad (1)$$

113 As the AFM-IR technique is based on photothermal excitation induced by the laser pulses, the
114 frequency of the heat modulation is directly given by the laser repetition rate or laser frequency.
115 Recent experiments using resonance enhanced AFM-IR (*12*, *13*) confirmed an increase in probing
116 depth with a decrease in laser repetition rate, although not following Eq (1) quantitatively.
117
118 Given the current lack of a detailed description of the probing depth, we propose a different
119 approach. In this paper, we first calibrate the probing depth on a model sample consisting of two
120 different polymers: polymethylmethacrylate (PMMA) and polystyrene (PS), forming a PS-PMMA
121 calibration wedge. This calibration then serves as the input for a tomographic reconstruction of the
122 sample of interest: a PS-PMMA blend (see Materials and Methods).
123
124 The PS-PMMA calibration wedge sample is made of a homogeneous PMMA film with a thickness
125 of about 18 µm onto which a 2 µm thick PS droplet of 200 µm diameter has been deposited
126 (Fig. 1A). The edge of the PS droplet forms a wedge of PS on the PMMA substrate and simulates
127 a well-defined, monotonic increase in PS sample thickness in the AFM-IR analysis. For the
128 calibration, the AFM cantilever is scanned perpendicularly to the PS wedge to avoid coupling of
129 lateral or torsional forces into the normal (vertical) force detection during the contact mode AFM
130 scan (Fig. 1B).
131

-Bruker Confidential-

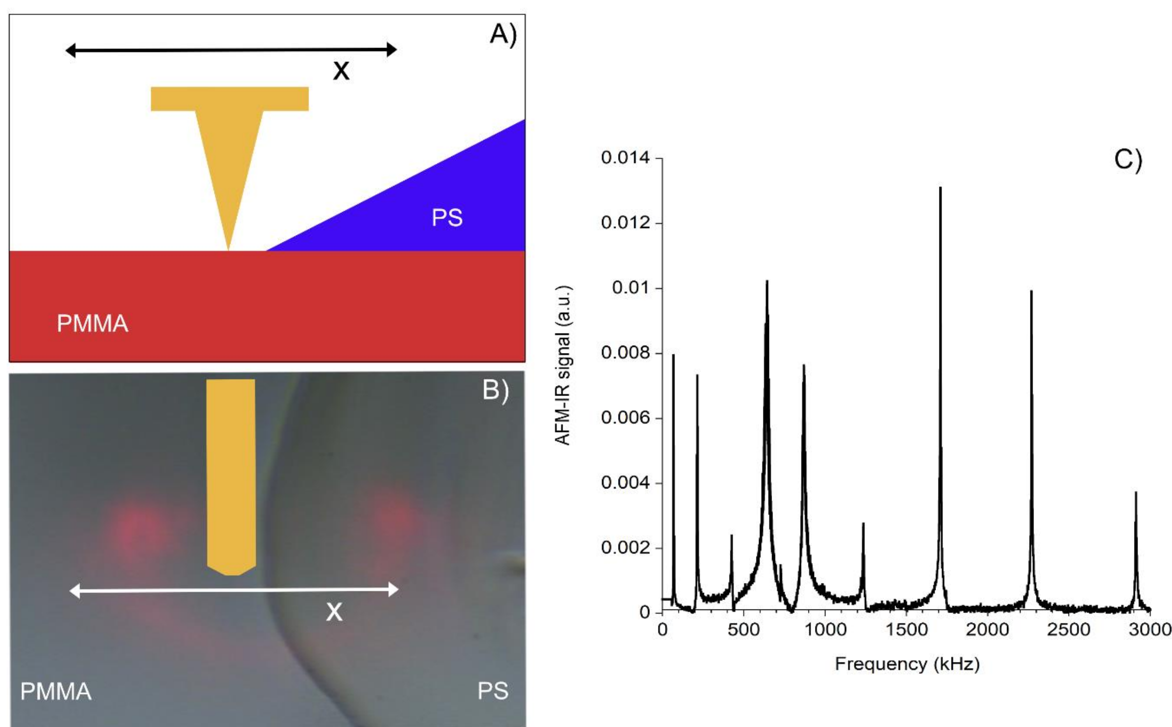

132
133 ***Fig. 1 Calibration sample and setup*** *A) Schematics of the tip and the PS wedge on the thick PMMA film.*
134 *B) Optical microscope image of the PS-PMMA calibration wedge sample. A sketch of the Au-coated*
135 *cantilever with the tip on the bottom end is shown and the arrows indicate the scan direction. C) Contact*
136 *resonance modes of the HQ cantilever in contact mode obtained on the PMMA film with the laser tuned to*
137 *the C=O absorption band at 1730 cm^{-1}. The modes are: 68 kHz, 213 kHz, 426 kHz, 644 kHz, 869 kHz,*
138 *1236 kHz, 1709 kHz, 2269 kHz, 2912 kHz.*
139
140
141 We describe in the following the depth calibration process. Resonance enhanced AFM-IR is the
142 employed technique that is later compared to surface sensitive and tapping AFM-IR. In our
143 resonance enhanced AFM-IR measurements, we selected a HQ:CSC38/Cr-Au (Mikromasch)
144 contact mode cantilever with 0.03 N/m spring constant and Cr-Au coating on both sides that can be
145 excited at 9 different contact resonance modes over the 0-3 MHz range (Fig. 1C). For all the
146 experiments, the calibration process is realized on the exact same location of the PS wedge to avoid
147 any variation of the absorption signal from topography (different slope) or change of mechanical
148 interaction between the tip and the sample. A phase locked loop (PLL) is activated to track any
149 change of the contact resonance during the AFM-IR scan, thus automatically adjusting the laser
150 repetition rate to always match the local contact resonance. Most of the time, the phase shift
151 corresponds to a cantilever resonance shift related to the mechanical contact change between the
152 PMMA and the PS surface. The use of a frequency-tracking mechanism is crucial in order to obtain
153 artifact-free AFM-IR signals that could otherwise overestimate the absorbance of either the PMMA
154 or PS domain. Furthermore, the choice of materials for wedge and substrate is critical for the most
155 accurate calibration of the probing depth. For example, using a substrate of silicon together with a
156 PMMA wedge leads to strong phase shifts that might challenge the PLL to correct properly,
157 resulting in an overestimated probing depth (Fig. S1). This large phase shift is directly related to
158 the fact that the Young's modulus of silicon is ~30 times greater than that of PS. This illustrates the
159 importance of a perfectly suited substrate to reduce the mechanical variation between the wedge
160 and substrate material. In all our experiments on the PS-PMMA calibration wedge sample, the PLL
161 easily corrects for the phase shift as their Young's moduli are close and equal to 3.1 GPa and 2.7
162 GPa for PMMA substrate and PS wedge, respectively. Only on the first nanometers of the tip of the

-Bruker Confidential-

163 PS wedge, the phase shift is not properly compensated by the PLL, probably because of a change
164 of lateral friction when passing from PMMA to PS (see Fig. S2). This very small fraction of the PS
165 wedge is systematically excluded in the probing depth analysis.
166
167 In the calibration process, we first scan for each cantilever mode (see Fig. 1C), i.e. laser repetition
168 rate, the topography together with the AFM-IR signal at 1730 cm^{-1} which is the main absorption
169 peak of the PMMA carbonyl band. Following the PMMA substrate absorption signal for a specific
170 cantilever mode along the wedge allows to evaluate at which depth, or PS thickness, the buried
171 PMMA can be detected by the AFM-IR technique, and then to estimate the probing depth of the
172 technique. Any tilt in the topography image of the exposed PMMA substrate area is corrected with
173 a plane fit. From the averaged line profiles across the wedge (10 lines were averaged, see Fig. 2A
174 and Fig. 2D for a laser repetition rate of 610 kHz and 1235 kHz, respectively) the height offset is
175 removed to arrive at the relation between the x axis position and the PS thickness. With the real PS
176 thickness as a function of the x-position, it is then possible to represent the simultaneously recorded
177 AFM-IR signal as a function of the PS thickness. Taking into account the imperfect correction of
178 the PLL due to friction as mentioned above, the first nanometers of (PS) thickness have been
179 removed from the graphs. As shown in the resulting Fig. 2C and Fig. 2F, representing respectively
180 the thickness dependent AFM-IR signals at 610 kHz and 1235 kHz, the behavior of the AFM-IR
181 signal is very well fitted by an exponential decrease law demonstrating that the thermal expansion
182 shows similarities to the exponential nature of the simplest form of Beer's law used in computed
183 tomography, as well as the penetration depth of microwave power. For all cantilever modes the
184 mathematical fit formula can be written as:

185 $$A(z) = m_1 + m_2\, e^{-\frac{z}{m_3}} \qquad (2)$$

186 Where z is the wedge thickness below the tip position, and m_1-m_3 are fit parameters.
187 As the stress created by the thermal expansion decreases exponentially with the distance (or
188 thickness), the probing depth may be defined as the exponential argument (m_3), at which the
189 AFM-IR signal decays to 1/e above an offset m_1. For these two example frequencies in Fig. 2C and
190 Fig. 2F, we can confirm that the probing depth decreases as the mode frequency increases: 292 nm
191 for 610 kHz and 125 nm for 1235 kHz

-Bruker Confidential-

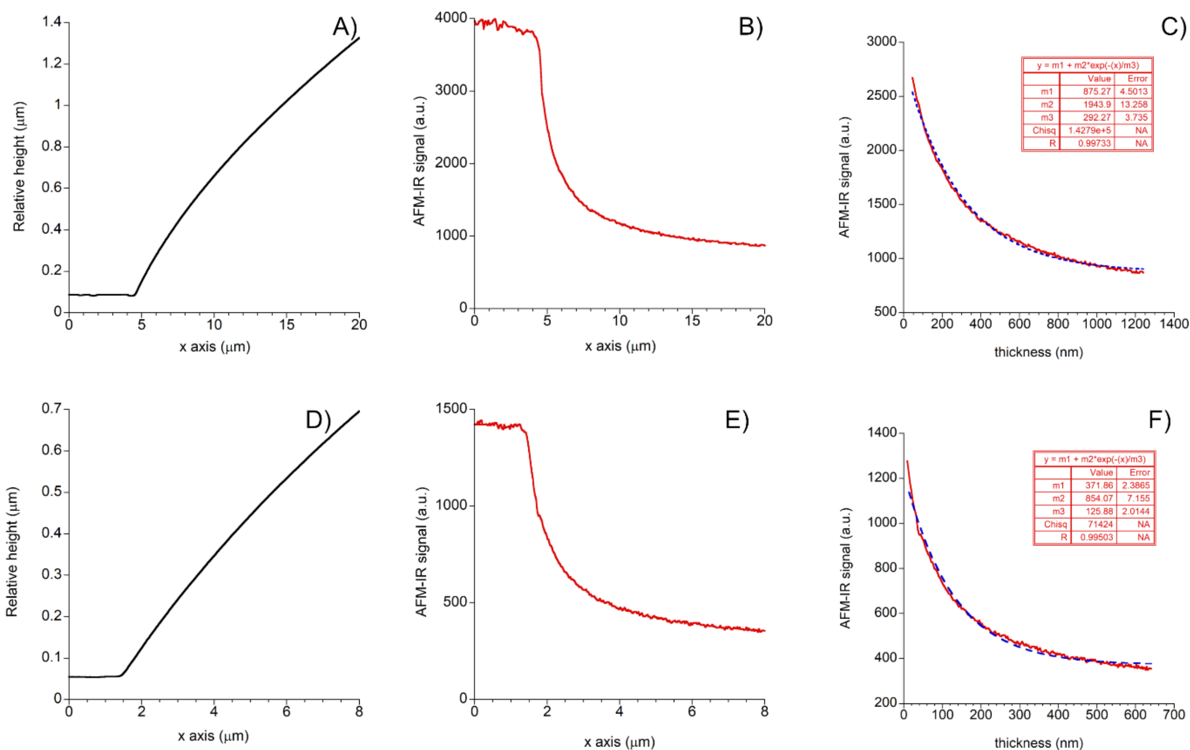

Fig.2 Methodology to estimate the probing depth of PMMA at 610 kHz and 1235 kHz. *A) Topography line profile of the PS wedge. B) Corresponding AFM-IR signal at 610 kHz for 1730 cm^{-1}. C) AFM-IR signal at 610 kHz as a function of PS thickness (red curve), the dashed blue curve represents the corresponding exponential fit. The table gives the fit values. D) Topography line profile of the PS wedge. E) Corresponding AFM-IR signal at 1235 kHz for 1730 cm^{-1}. F) AFM-IR signal at 1235 kHz as a function of PS thickness (red curve), the dashed blue curve represents the corresponding exponential fit. The table gives the fit values.*

The same study is repeated using the PS absorption band at 1600 cm^{-1} to evaluate the probing depth for top-layer absorption (Fig. 3) compared to the previous buried substrate absorption (PMMA, Fig. 2). The difference of this new case is that the tip is now directly on the expanding sample when on the PS. Opposite to probing the buried PMMA substrate before, we now observe an AFM-IR signal increase with increasing PS wedge thickness. The aromatic C=C absorption band of PS is much weaker than the carbonyl C=O absorption band of PMMA. To compensate for this difference in absorption strength, the laser power has been increased to 4.9% (instead of 0.5% for PMMA). The data treatment follows the exact same procedure as before (tilt removal and offset correction of the topography) but the fit function used to describe the AFM-IR signal of the PS droplet is now given by the following expression:

$$A(z) = m_1 + m_2\left(1 - e^{-\frac{z}{m_3}}\right) \qquad (3)$$

Where z is the wedge thickness at the tip position, and m_1-m_3 are fit parameters.

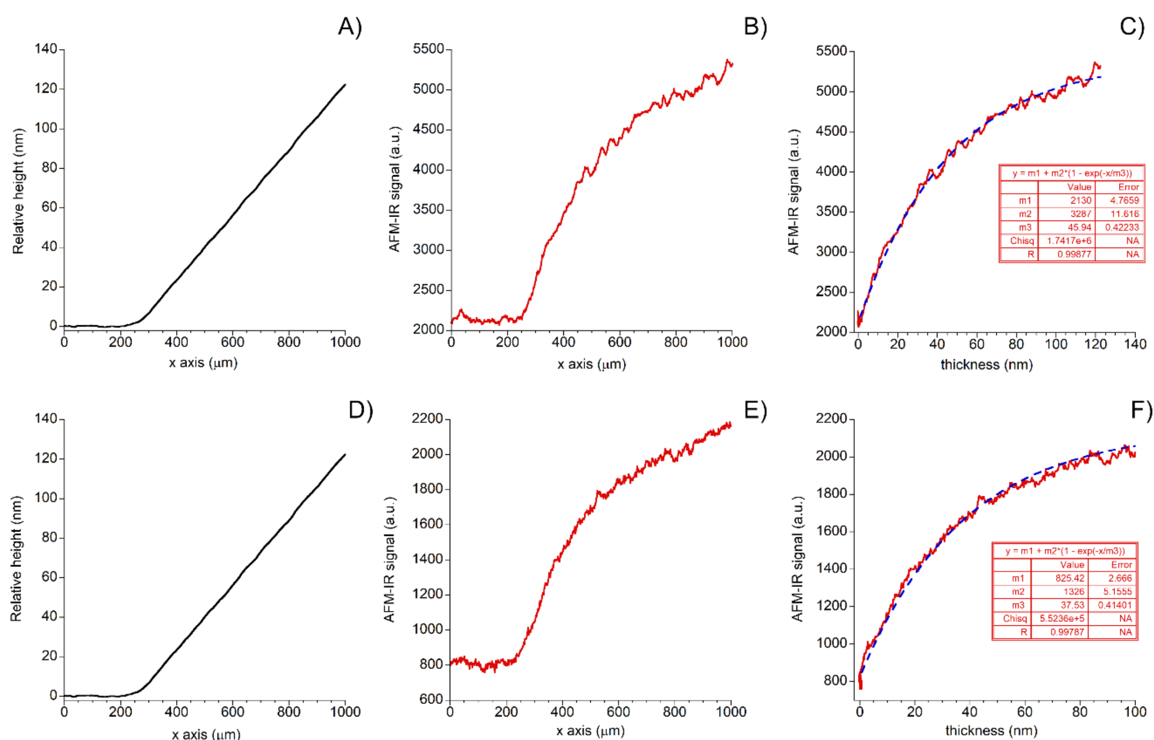

218
219 **Fig. 3** ***Methodology to estimate the probing depth of PS***. *A) Topography line profile of the PS wedge. B)*
220 *Corresponding AFM-IR signal at 2272 kHz for 1600 cm^{-1}. C) AFM-IR signal at 2272 kHz as a function of*
221 *PS thickness (red curve) and exponential fit (dashed blue curve). Fit parameters are given in the table. D)*
222 *Topography line profile of the PS wedge. E) Corresponding AFM-IR signal at 2915 kHz for 1600 cm^{-1}. F)*
223 *AFM-IR signal at 2915 kHz as a function of PS thickness (red curve) and exponential fit (dashed blue curve).*
224 *Fit parameters are given in the table.*
225
226
227 **Probing depth calibration in resonance enhanced contact mode AFM-IR**
228
229 Above calibration procedure is carried out for all 9 accessible contact resonances (Fig. 1C) of the
230 Mikromasch HQ probe in resonance enhanced AFM-IR. The probing depth, i.e. fit parameter m_3
231 in Eq (2) for PMMA and (3) for PS, respectively, is reported in Fig. 4 as a function of the laser
232 frequency.

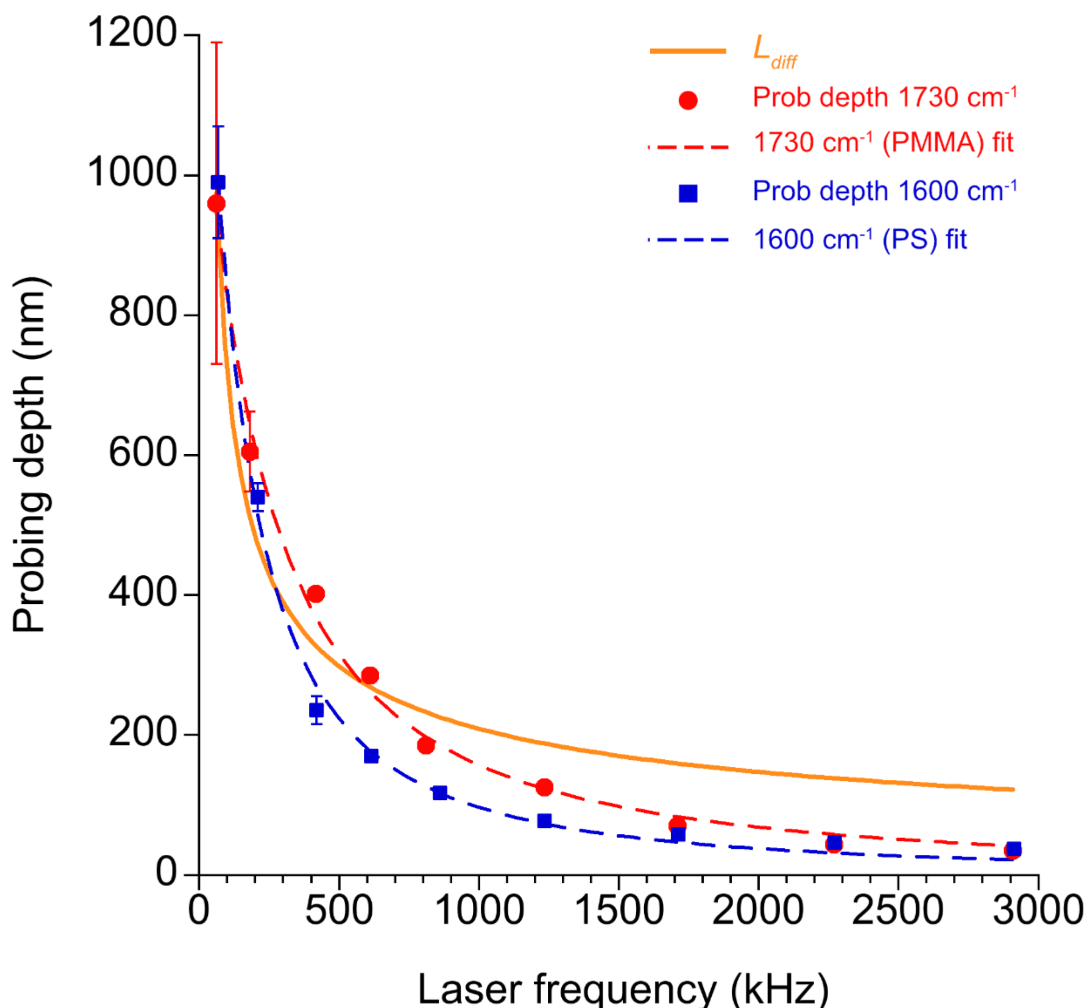

233
234 **Fig. 4 *Probing depth as a function of the laser frequency*.** *PMMA is represented by red dots and PS by*
235 *blue squares, error bars are represented in the corresponding color, the dashed curves indicate the*
236 *corresponding fits and the orange curve corresponds to the thermal diffusion length.*
237
238 The obtained curves for PMMA and PS are compared to the thermal diffusion length defined by the power
239 law of Eq. (1) with a power-law exponent of -1/2. The comparison clearly shows that the decrease of
240 experimental probing depth as a function of the laser frequency is much faster than for a power law exponent
241 of -1/2 for the thermal diffusion length. The best fit function found to describe this behavior can be expressed
242 by the formula below and table 1 reports the fitted values for PMMA and PS with both a correlation
243 coefficient R=0.998:
244
245 $$PDepth(f) = \frac{a}{(f-b)^c} \qquad (4)$$
246
247 Where f is the laser frequency
248

	PMMA	PS
a	$2.4\ 10^{11}$	$2.9\ 10^{11}$
b (Hz)	-343 000	-200 000
c	1.499	1.55

249 ***Table 1 : Fitted values for PMMA and PS.***
250

251 The power argument (c) extracted from the fit function (4) for both cases seems to be close to -3/2. This
252 could be explained by the fact that the total transfer function is simply the product between the thermal
253 diffusion (power law exponent -1/2) and the response of the cantilever (exponent -1). The extrapolation of
254 these laws to a laser frequency of 1 kHz allows us to predict the probing depth of the first AFM-IR
255 implementation (not resonantly-enhanced) using a low-repetition rate OPO laser. The probing depth are
256 respectively 1.2 µm for PMMA and 1.56 µm for PS. These values are in good agreement with the 1 µm
257 range of linearity experimentally estimated by Centrone and coworker using a PMMA wedge on zinc
258 selenium (*14*). Indeed, the range of linearity of the contact mode must be much smaller than the probing
259 depth and correspond to the range where the exponential decay can be fitted by a linear dependency.
260
261
262 **Probing depth calibration in surface sensitive AFM-IR and tapping AFM-IR mode**
263
264 Surface sensitive AFM-IR is a relatively new operating mode that allows one to reduce drastically
265 the probing depth of contact mode (*12*). The calibration in this previous work has been realized on
266 a sample (polyurethane on silicon substrate) not specifically designed to avoid mechanical artifacts.
267 The methodology described in the previous paragraph is used to reevaluate the probing depth on
268 the optimized PS-PMMA calibration wedge. The mechanical oscillation of the tip is fixed at 3 MHz
269 and generated by the piezo actuator (the one typically used in AFM tapping mode). The laser
270 frequency is tuned to match the difference of piezo and laser frequencies with a contact resonance
271 mode of the cantilever. This frequency mixing approach is similar to DFG (difference frequency
272 generation) and possible only because the tip-surface interaction is non-linear (*12*).
273 The probing depth of the surface sensitive mode is represented in Fig.5.

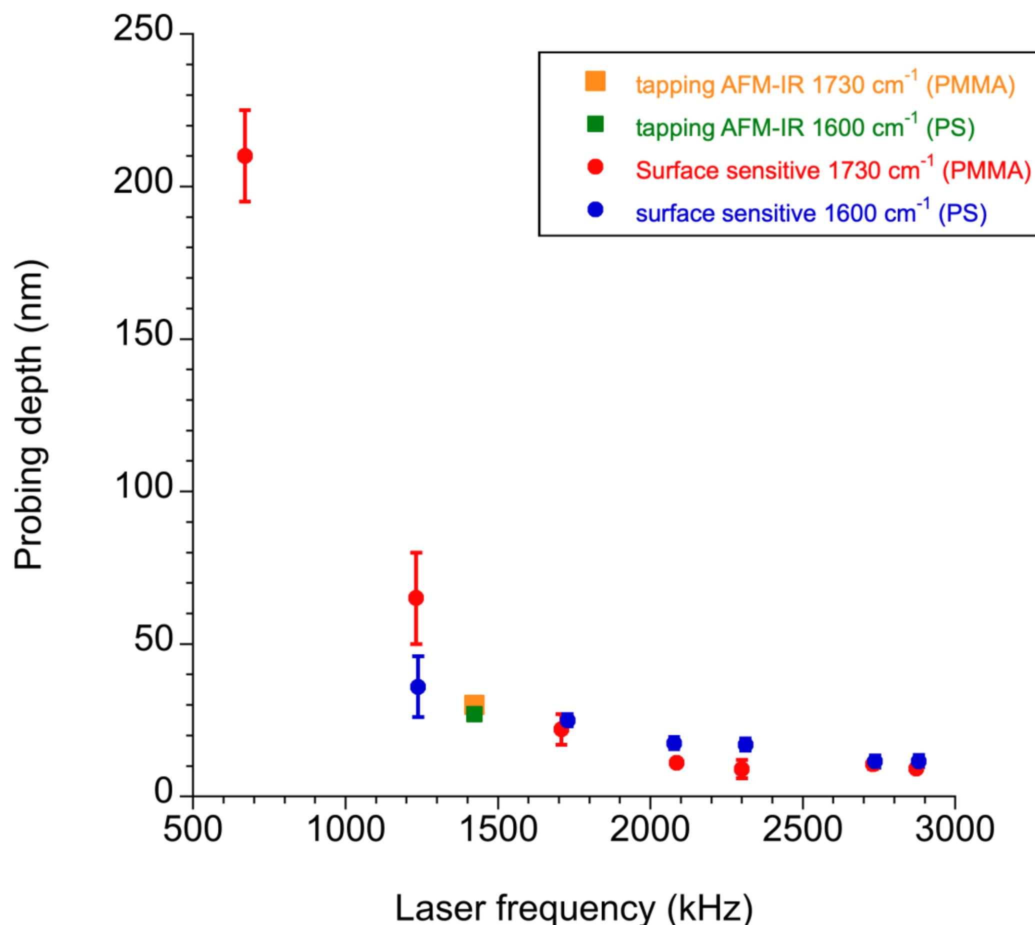

274
275 ***Fig. 5 Surface sensitive probing depth as a function of the laser frequency**. Red and blue data points*
276 *represent respectively the results for PMMA and PS for surface sensitive AFM-IR. Error bars are*

represented in corresponding colors. Orange and green squares represent the probing depth of the tapping AFM-IR mode for PMMA and PS, respectively.

The probing depth of the surface sensitive mode seems to be equivalent for both PS and PMMA polymers at high laser frequencies. Note that in our experiment the PLL is activated and compensates perfectly for mechanical effects at the interface of the two polymers.
Furthermore, during the experiment, it was also quite difficult to go below a 1 MHz laser frequency because of instabilities in the IR signal. But even in this limited laser frequency range, we can see that the probing depth decreases from 50 nm to 10 nm. The quality of the wedge is still a limitation to the accuracy of this experiment. The first nanometers of the wedge are important for a good estimation of the probing depth as we need nanometer sensitivity. This is why an improved design of the wedge more adapted for small thicknesses should give us a more accurate view of the evolution of the probing depth in the range of 2 MHz -3 MHz.

Tapping AFM-IR mode is also a surface sensitive mode. The only difference is that instead of modulating the tip motion continuously on the surface in constant contact with the sample (contact resonance), the tip is now in intermittent contact in tapping AFM-IR. Based on the same non-linear interaction, the theory used to describe the measurement is the same for both cases(*12*, *15*, *16*). Using the same PS-PMMA calibration sample as for the surface sensitive and resonance enhanced AFM-IR; the probing depth has been evaluated for a 300 kHz tapping gold coated cantilever PPP-NCHAu-MB-10 from Nanosensors (Fig.5). The cantilever mode used for the piezo drive was fixed at 1694 kHz and the mode to detect the IR signal was fixed at 272 kHz. In order to minimize mechanical induced artifacts during scanning, two PLLs were used to track both the tapping frequency and the IR detection frequency. The probing depth evaluated under these conditions is about 30 nm (Fig.S3) which is considerably smaller than our previous evaluation of 50 nm for the polyurethane wedge on Si substrate (*12*). This confirms the necessity to apply the same and correct methodology to compare the probing depth properties of different polymer nature. At the same laser frequency, the probing depth for tapping AFM-IR matches well with the probing depth for surface sensitive AFM-IR attesting that the physics involved in the non-linear interaction is the same.

Compared to the data presented in Fig. 4 for resonance enhanced AFM-IR, surface sensitive AFM-IR and tapping AFM-IR provide a smaller probing depth (i.e. higher surface sensitivity) at equivalent laser frequencies. We attribute this to the non-linear interaction for the latter two modes.

Tomography reconstruction

After above depth calibration, we now turn to its application of subsurface sensing in tomography. The sample used to illustrate the potential of tomography reconstruction is a blend of PS-PMMA presented in the material and method section. This sample is a matrix of PMMA of 1.9 µm thickness wherein PS droplets of different sizes are embedded. The mode of operation is resonance enhanced AFM-IR. Using the exact same HQ:CSC38/Cr-Au cantilever as for the calibration, we have recorded the chemical maps at 1730 cm^{-1} corresponding to the ester carbonyl absorption band of PMMA for all the contact resonance modes from 50 kHz to 3 MHz (9 modes, Fig. 1C). Figure 6 represents these chemical maps of the same area where the darker PS domains are surrounded by a bright, absorbing PMMA matrix (corresponding topography in Fig. S4).

-Bruker Confidential-

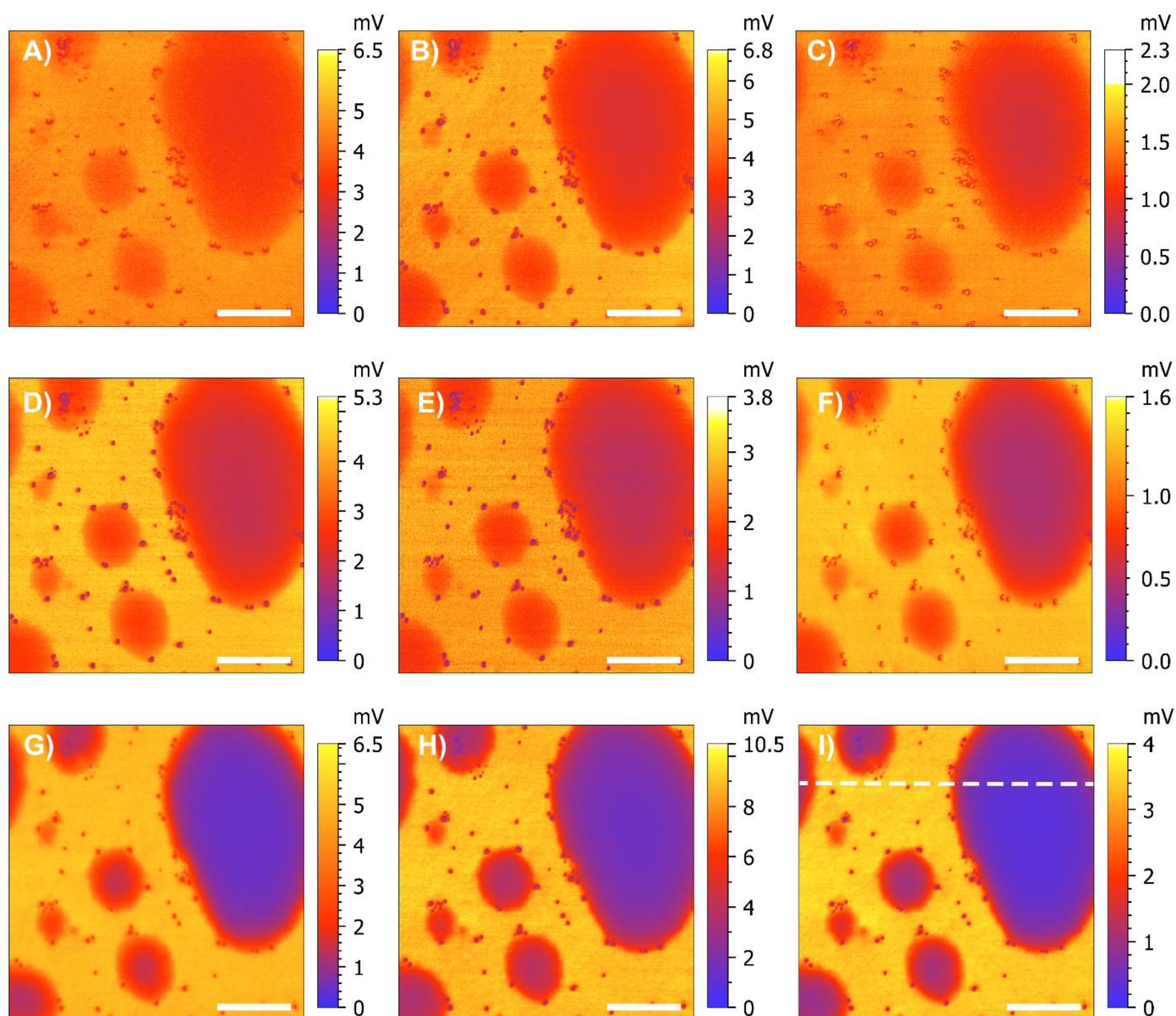

322
323 ***FIG. 6 : Chemical maps of the PS-PMMA blend at the ester carbonyl absorption band of PMMA***
324 ***(1730 cm^{-1}) for all the contact resonance modes.*** *A) Laser frequency 68 kHz. B) 212 kHz. C) 417 kHz. D)*
325 *620 kHz. E) 870 kHz. F) 1235 kHz. G) 1705 kHz. H) 2275 kHz. I) 2911 kHz. The white scale bar corresponds*
326 *to 750 nm.*
327
328 The mixing of PS and PMMA resembles the one of oil and water, respectively, where PS similar
329 to oil minimizes its thickness while floating on PMMA. The full thickness of the PMMA matrix is
330 1.9 µm which is larger than the expected thickness of the PS droplet. Consequently, there should
331 be a non-negligible amount of PMMA below all the PS droplets. In the measurements presented in
332 Fig. 6, we clearly see that when the laser frequency increases, the signal contrast between the PS
333 droplets compared to the PMMA matrix also increases, i.e. while PS and PMMA areas show a
334 nearly comparable signal strength at 68 kHz, the PMMA signal at 2911 kHz in PS droplet is greatly
335 reduced. The increase of PS contrast is directly related to the probing depth: as the laser frequency
336 increases, the amount of PMMA seen below the PS decreases and the resulting contrast increases.
337 Note that, based on the obtained PS contrast that appears relatively uniform within each droplet,
338 the droplets seem to be not spherical but rather shaped more like puddles. We can also detect very
339 small nanoparticles that are not absorbing at 1730 cm^{-1} with a size about 50 nm diameter (Fig. S4
340 and S5). These nanoparticles are neither PS nor PMMA but some contamination of the PMMA
341 solvent and have a strong carbonyl absorption band around 1650 cm^{-1} (Fig. S5).
342

-Bruker Confidential-

343 To reconstruct a 3D tomogram of our sample, it is necessary to express the AFM-IR intensity
344 analogue to Eq. (2) and include the thickness of PS as a function of the position x,y on the surface:
345
346
$$I(x,y,f_n) = I_0(f_n)e^{-z(x,y)/p_n} \quad (5)$$
347
348 Here, $I_0(f_n)$ corresponds to the AFM-IR signal on pure PMMA (z=0) for a cantilever contact
349 resonance frequency f_n, z(x,y) is the thickness of PS at the position x,y (z=0 on pure PMMA), and
350 p_n is the probing depth, evaluated in the previous paragraph, at frequency f_n. This expression is
351 valid only for the case of PMMA absorption and PS on the top which correspond to the IR maps
352 resented Fig.6.
353
354 In order to reconstruct the tomogram, i.e. the three-dimensional sub-surface distribution of the PS-
355 PMMA blend, we can use the inverse transformation of Eq. (5) for each pixel of the AFM-IR maps,
356 and for each resonance of the cantilever:
357
358
$$z(x,y) = -p_n ln\left(\frac{I(x,y,f_n)}{I_0(f_n)}\right) \quad (6)$$
359
360 We assume that there is no PMMA layer on the PS samples. This is confirmed by the surface
361 sensitive maps (Fig. S6.) that give zero level of absorption at 1730 cm^{-1}, meaning that the top
362 surface of PS sample is only PS. Applying this inverse transformation on the cross section through
363 the large PS droplet (white dashed line in Fig. 6I) for all the contact resonance modes we obtain the
364 reconstruction of the PS droplet shape in depth or thickness z (Fig. 7). Our previous calibration data
365 obtained at 1730 cm^{-1} (PMMA absorbs) in Fig. 4 entered as the probing depth p_n (see the
366 corresponding values in the legend of Fig. 7).
367

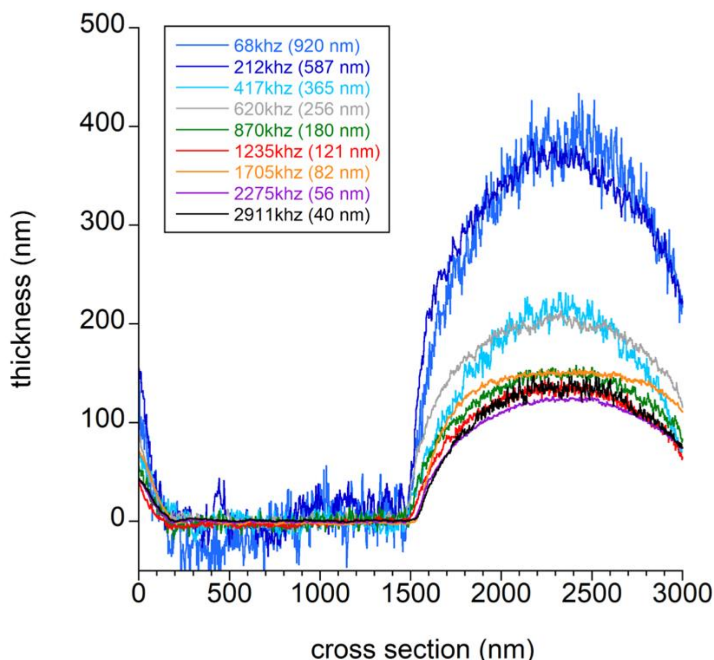

368
369 ***Fig.7 : Tomography reconstruction of the PS droplet***. The calculated thickness profile of the large PS
370 droplet, at the position of the white dashed line cut in Fig. 6I, is represented as a function of each
371 cantilever contact mode (different colors). For each mode the value of the corresponding probing depth is
372 given in brackets (taken from Fig. 4 for the 1730 cm^{-1} calibration data).
373

-Bruker Confidential-

With this reconstruction we clearly demonstrate that the 4 first modes (68 kHz – 620 kHz) are not suited for the tomography reconstruction of this sample because they do not converge to the same value as for the higher modes. Since the thickness of PMMA is finite (1.9 µm) these 4 low-frequency modes probe below the PMMA layer and interact with the underlaying silicon substrate. This sampled silicon volume is not absorbing at 1730 cm^{-1}, therefore, does not contribute to an AFM-IR signal in the same way as a thicker PS droplet would. Hence, these 4 lower modes overestimate the PS thickness. Moreover, the lower modes have lower lateral resolution and therefore also interact with the surrounding PMMA. For frequencies equal and higher than 870 kHz, the calculated PS droplet thickness seems to converge around a thickness of 138 nm for the line profiles of Fig. 7. Consequently, the reconstruction can be applied to the entire scan of the surface by considering only these higher modes from 870 kHz to 2911 kHz and averaging the 5 corresponding images. This gives a good approximation of the size of the PS droplet with a small error induced by this type of reconstruction.

This averaged reconstruction of the 1730 cm^{-1} maps revealing the three-dimensional shapes of the PS droplets is represented in Fig. 8.

-Bruker Confidential-

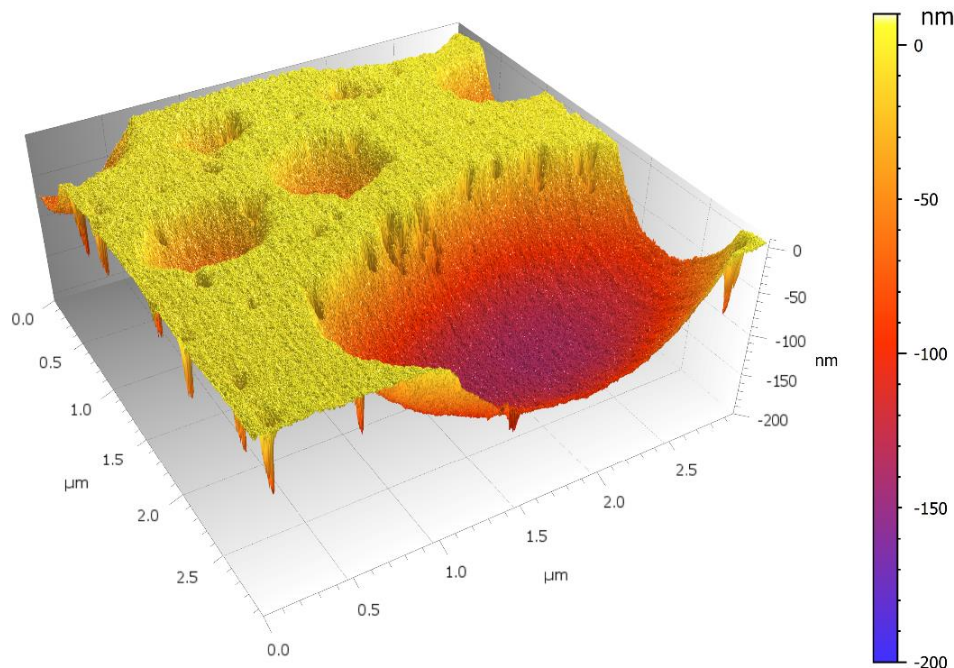

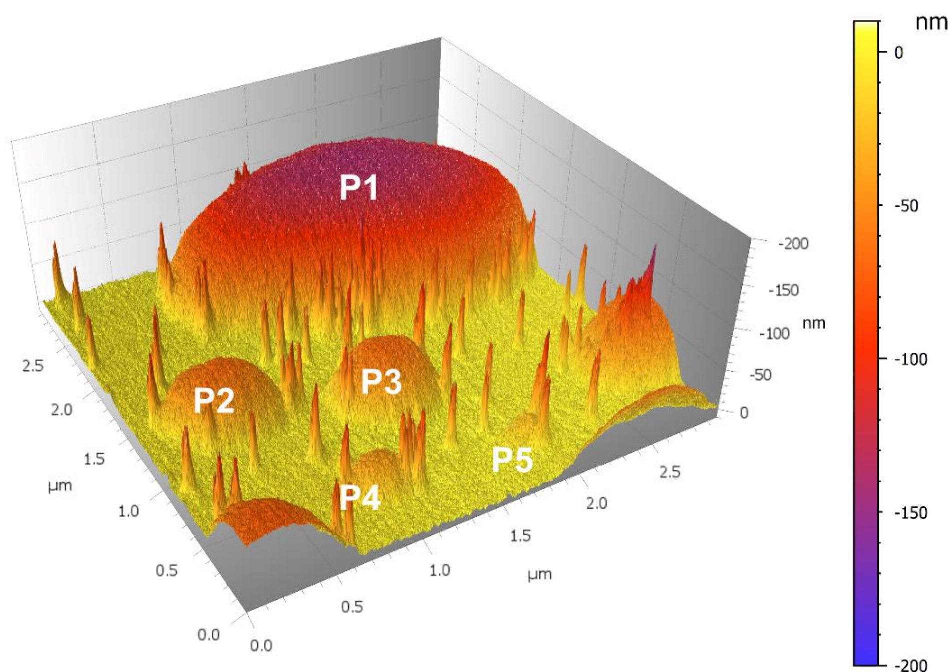

Fig. 8 : 3D representation of the PS-PMMA blend. *A) 3D representation revealing the size & thickness of PS droplets . B) Same data as in A) but with inverted z-axis and rotated for clarity. Some PS droplets are labelled P1-P5.*

We can clearly distinguish several droplets that are in fact shaped more like puddles than droplets as the thickness is around one hundred nanometers or less at a size of a few micrometers. The accuracy of the calculated thickness is estimated by the analysis of all the modes and reveals a quite good standard deviation of a few nanometers. Table 2 summarizes the maximum thickness of a few puddles (P1-P5) indicated in Fig. 8B.

	P1	P2	P3	P4	P5

-Bruker Confidential-

Averaged thickness (nm)	138	53	58	37	22
Error (nm)	6	5	6	6	3

Table 2 : Thickness of representative PS droplets from Fig. 8B.

We can also observe in Fig. 8 that the nanoparticle surface contaminants have a characteristic thickness of about 70 nm for a diameter of around 60 nm and a height of 10 nm. The thickness value is probably overestimated because the probing depth calibration has been realized with PS and not with the contaminant. We can observe that the constraint of the outlined 3D reconstruction procedure is limited to give reliable depth information only for those materials that were used for the probing depth calibration, i.e. here, the PMMA matrix and the embedded PS droplets.

So far, we utilized the depth calibration based on the 1730 cm^{-1} PMMA absorption, see Fig. 4. Carrying out the 3D tomography reconstruction of PS based on the depth calibration data obtained at the 1600 cm^{-1} PS absorption (Fig. 4) for an image of the PS-PMMA blend taken at 1600 cm^{-1} is more complicated. Analogue to Eq. (6) we can derive an expression for the position-dependent PS thickness z:

$$z(x,y) = -p_n ln\left(1 - \frac{I(x,y,f_n)}{I_{0_PS}(f_n)}\right) \quad (7)$$

Now, $I_{0_PS}(f_n)$ corresponds to the AFM-IR signal on pure PS (z=0). While before, the AFM-IR signal on pure PMMA, $I_0(f_n)$, was accessible in the 1730 cm-1 scans (Fig. 6) due to the thick PMMA matrix, $I_{0_PS}(f_n)$ cannot be estimated from the 1600 cm-1 scans since its value corresponds to an infinite PS thickness, or a PS thickness much larger than the probing depth. But the thickest PS droplet is only ~138 nm thin and hence there is no way to estimate the value $I_{0_PS}(f_n)$ for the given cantilever modes. $I_{0_PS}(f_n)$ can be an adjustable parameter to converge to the estimated thickness of the P1 droplet, the 138 nm reconstructed from the PMMA absorption scans. The 3D reconstruction with PS absorption maps is represented in SI (Fig S7) but does not give any additional information compared to the previous 3D tomography for the PMMA absorption.

Discussion

In this work we have described a robust methodology to calibrate the probing depth of AFM-IR imaging modes (contact, surface sensitive and tapping). With this calibration it was then possible to reconstruct in 3D the tomography of a polymer blend and hence to determine the sub-surface 3D shape of polystyrene puddles in a polymethacrylate matrix.
The calibration presented here has only been realized for a single cantilever but it would be interesting in a next step to repeat with cantilevers from the same batch to learn about their statistical dispersion and see the possibility to establish a more general calibration curve. Other AFM-IR cantilever types and brands can also be characterized regarding their probing depth. This type of study would be long and fastidious, but it would surely be very useful for the community to obtain such reference values for the probing depth for a known polymer. Our work here only concerns PS and PMMA but the method is applicable to other polymers as well, as they can have orthogonal solvents for the drop cast preparation, or one can imagine other ways to create a clean calibration wedge. We have seen that the wedge obtained with the drop cast method is not optimal for surface sensitive AFM-IR as we need a smaller slope of the wedge to get a better estimation for the smaller

-Bruker Confidential-

445 probing depths (10-20 nm). However, the drop cast wedge is still a good standard to evaluate the
446 probing depth of contact mode of any kind of polymer material.
447 We have also pointed out that it is crucial to minimize any mechanical impedance between the
448 calibration wedge and its substrate to obtain a good estimation of the probing depth. However, the
449 calibration wedge must also be matched to the material system for which the 3D tomography
450 reconstruction is carried out. For example, the calibration data for a PMMA wedge on a Si substrate
451 proved inadequate for our PS-PMMA blend but could be useful for other situations where the
452 sample is deposited on Si substrate. This necessity to design a suitable wedge for each sample of
453 interest is a limitation of the presented calibration procedure.
454 The calibration methodology developed in this study (wedge-substrate analysis) allows an
455 estimation of the probing depth for an expanding sample, buried or not. For this, we assume that
456 the signal at the wedge position (i.e. a given thickness of PS) is perfectly equivalent for a flat layer
457 of the same thickness in bulk. The probing depth was defined as an AFM-IR signal drop to 1/e
458 (~37%), i.e. it captures 63% of the AFM-IR signal, but it does not give the range in which the
459 technique is able to "feel" the sample. A sampling depth could be defined as 3 times the probing
460 depth to comprise 95% of the AFM-IR signal, which would be an alternative representation of the
461 depth sensitivity of the respective cantilever mode. Turning to Fig. 4, the empirical law from our
462 measurement fits very well the behavior of the cantilever modes and the sampling depth can be
463 easily evaluated as a function of the mode frequency: at 3 MHz the sampling depth is around
464 150 nm and for 200 kHz it is 3 µm. This law should be only dependent on the laser frequency, and
465 neither on the power nor the pulse duration. Further work is required to fully map out th impact of
466 all the laser parameters on the probing depth.
467 The empirical law is a power law with an exponent of -3/2 which is different from -1/2 for the
468 classical thermal law. This is probably related to the fact that we are measuring a photothermal
469 expansion and this phenomenon is not only thermal but also mechanical, i.e. the transfer function
470 between tip and cantilever has also a strong influence.
471 The outlined probing depth calibration procedure allowed us to introduce a novel application of the
472 AFM-IR technique: 3D tomography with sub-surface imaging. We have shown how to reconstruct
473 the three-dimensional shape of PS puddles in a PMMA matrix of a PS-PMMA blend with very
474 good accuracy (only a few nanometers of error). This 3D reconstruction is only possible using a
475 calibration sample with a PMMA matrix covered by a PS wedge. Furthermore, successful 3D
476 tomography requires to calibrate the probing depth based on the matrix (i.e. PMMA) AFM-IR
477 absorption signal: The lack of absorption reveals the real shape of the embedded material (PS)
478 inside the matrix. Calibration based on the PS wedge absorption proved less successful to
479 reconstruct the 3D shape of the sample of interest since its surface contains no PS puddles of infinite
480 or very large thickness (with respect to the probing depth) that are required by the reconstruction
481 formula. As another drawback, this 3D tomography is currently not applicable to all samples and
482 will be restricted to binary blends. We have not yet devised an experiment to reconstruct a ternary
483 blend, for example 2 different embedded polymers inside another matrix polymer.
484
485 Irrespective of the mentioned potential limitations, the 3D tomography is a property only reserved
486 for the AFM-IR technique as it is a photothermal measurement in which the perfect control of the
487 probing depth allows the depth investigation. This approach is not possible in sSNOM even if many
488 works have shown 3D maps of electromagnetic fields of the tip-sample interaction (*17*). The
489 scattering of the light by the tip is imposed by its shape and there is currently no practical way to
490 change the evanescent wave generated by the tip to modulate the electric field probing depth which
491 is around 10-50 nm (*18*). The biggest advantage of AFM-IR is its flexibility to probe in a depth
492 ranging from several micrometers to a few nanometers just by changing the laser frequency from
493 tens of kHz to a few MHz.
494

-Bruker Confidential-

Materials and Methods

Sample preparation

Polymethylmethacrylate (PMMA) (150 kDa) and polystyrene (PS) (50 kDa) were purchased from Sigma-Aldrich. Those polymers were chosen for their comparable mechanical rigidity properties (Young's modulus is respectively 3.1 and 2.7 GPa) while having very different chemical structures. Both are soluble in tetrahydrofuran (THF) while only PS is soluble in cyclohexane.
Various solutions were prepared: a blend of PS and PMMA in THF with a concentration of 10 mg/mL, a solution of PMMA in THF with a concentration of 10 mg/mL, and a solution of PS in cyclohexane with a concentration of 1 mg/mL.
Sample preparation involved the solvent casting method. The PS-PMMA blend and the PMMA solutions were dropped on a silicon wafer under a controlled atmosphere. Subsequently, for the PS wedge on PMMA samples, a few droplets of PS solution were deposited over the PMMA thin film. The samples were then annealed at 125°C for 6 hours after each step of the deposition to remove all traces of solvent. By using this simple method, the polymer layer thicknesses are about a few micrometers.

AFM

The AFM-IR system is a Dimension IconIR from Bruker with an infrared tunable QCL laser from Daylight Solutions covering the 1900-900 cm^{-1} range. The pulse length is fixed at 100 ns for all the experiments. Power is fixed at 0.5% for the PMMA analysis at 1730 cm^{-1}, and at 4.9% for PS at 1600 cm^{-1}. The cantilever used in resonance enhanced AFM-IR (contact mode) and surface sensitive AFM-IR is a cantilever from Mikromasch: HQ:CSC38/Cr-Au with CR/Au coating on both sides and a spring constant of 0.03 N/m. The cantilever used for tapping AFM-IR is from Nanosensors reference PPP-NCHAu-MB-10. Method is also applicable to alternative probe models.

Imaging analysis

Imaging analysis and treatment has been done by MountainsMap software (version 9) from Digital Surf.

References

1. A. Centrone, Infrared Imaging and Spectroscopy Beyond the Diffraction Limit. *Annual Review of Analytical Chemistry* **8**, 101–126 (2015).
2. A. Dazzi, C. B. Prater, AFM-IR: Technology and Applications in Nanoscale Infrared Spectroscopy and Chemical Imaging. *Chem Rev* **117**, 5146–5173 (2017).
3. M. Tabib-Azar, Y. Wang, Design and fabrication of scanning near-field microwave probes compatible with atomic force microscopy to image embedded nanostructures. *IEEE Trans Microw Theory Tech* **52**, 971–979 (2004).
4. K. Lai, M. B. Ji, N. Leindecker, M. A. Kelly, Z. X. Shen, Atomic-force-microscope-compatible near-field scanning microwave microscope with separated excitation and sensing probes. *Review of Scientific Instruments* **78** (2007).
5. E. Chilla, T. Hesjedal, H.-J. Fröhlich, Nanoscale determination of phase velocity by scanning acoustic force microscopy. *Phys Rev B* **55**, 15852–15855 (1997).
6. U. Rabe, W. Arnold, Acoustic microscopy by atomic force microscopy. *Appl Phys Lett* **64**, 1493–1495 (1994).
7. K. Yamanaka, H. Ogiso, O. Kolosov, Ultrasonic force microscopy for nanometer resolution subsurface imaging. *Appl Phys Lett* **64**, 178–180 (1994).

-Bruker Confidential-

8. G. Stan, C. V. Ciobanu, S. W. King, Resolving the Subsurface Structure and Elastic Modulus of Layered Films via Contact Resonance Atomic Force Microscopy. *ACS Appl Mater Interfaces* **14**, 55238–55248 (2022).
9. K. Kaja, A. Assoum, P. De Wolf, F. Piquemal, A. Nehmee, A. Naja, T. Beyrouthy, M. Jouiad, 3D Imaging and Quantitative Subsurface Dielectric Constant Measurement Using Peak Force Kelvin Probe Force Microscopy. *Adv Mater Interfaces*, doi: 10.1002/admi.202300503 (2023).
10. C. Plassard, E. Bourillot, J. Rossignol, Y. Lacroute, E. Lepleux, L. Pacheco, E. Lesniewska, Detection of defects buried in metallic samples by scanning microwave microscopy. *Phys Rev B* **83**, 121409 (2011).
11. P. Vitry, E. Bourillot, C. Plassard, Y. Lacroute, E. Calkins, L. Tetard, E. Lesniewska, Mode-synthesizing atomic force microscopy for 3D reconstruction of embedded low-density dielectric nanostructures. *Nano Res* **8**, 2199–2205 (2015).
12. J. Mathurin, A. Deniset-Besseau, D. Bazin, E. Dartois, M. Wagner, A. Dazzi, Photothermal AFM-IR spectroscopy and imaging: Status, challenges, and trends. *J Appl Phys* **131** (2022).
13. L. Quaroni, Understanding and Controlling Spatial Resolution, Sensitivity, and Surface Selectivity in Resonant-Mode Photothermal-Induced Resonance Spectroscopy. *Anal Chem* **92**, 3544–3554 (2020).
14. G. Ramer, V. A. Aksyuk, A. Centrone, Quantitative Chemical Analysis at the Nanoscale Using the Photothermal Induced Resonance Technique. *Anal Chem* **89**, 13524–13531 (2017).
15. J. Mathurin, E. Pancani, A. Deniset-Besseau, K. Kjoller, C. B. Prater, R. Gref, A. Dazzi, How to unravel the chemical structure and component localization of individual drug-loaded polymeric nanoparticles by using tapping AFM-IR. *Analyst* **143**, 5940–5949 (2018).
16. J. Mathurin, A. Deniset-Besseau, A. Dazzi, "Advanced infrared nanospectroscopy using photothermal induced resonance technique, AFMIR: New approach using tapping mode" in *Acta Physica Polonica A* (Polish Academy of Sciences, 2020)vol. 137, pp. 29–32.
17. H. Wang, L. Wang, D. S. Jakob, X. G. Xu, Tomographic and multimodal scattering-type scanning near-field optical microscopy with peak force tapping mode. *Nat Commun* **9** (2018).
18. T. Taubner, F. Keilmann, R. Hillenbrand, Nanoscale-resolved subsurface imaging by scattering-type near-field optical microscopy. *Opt Express* **13**, 8893 (2005).

Acknowledgments

The authors acknowledge Digital Surf for Mountains software support. This work was supported by the Paris Ile-de-France Region-DIM "Matériaux anciens et patrimoniaux.

Author contributions:

Conceptualization & methodology: A. D.
Sample prep: P. L, P. N. and Q. H.
Experiments: A. D.
Writing—original draft: A. D., J. M., P. D.W., M. W. and Q. H.
Writing—review & editing: all authors

Competing interests: Peter De Wolf, Martin Wagner and Qichi Hu are employed by Bruker Nano Surfaces Division, a manufacturer of instrumentation for AFM-based infrared spectroscopy. Alexandre Dazzi is a coinventor of AFM-IR patents licensed to Bruker Nano Surfaces Division. The other authors state no conflict of interest.

-Bruker Confidential-

600 **Data and materials availability:** All data, code, and materials used in the analyses must be
601 available in some form to any researcher for purposes of reproducing or extending the
602 analyses. Include a note explaining any restrictions on materials, such as materials transfer
603 agreements (MTAs). Include accession numbers to any data relevant to the paper and
604 deposited in a public database; include a brief description of the dataset or model with the
605 number. The DMA statement should include the following: "All data are available in the
606 main text or the supplementary materials."
607
608
609
610 **Supplementary Materials**
611
612 Please use the *Science Advances* template to format your Supplementary Materials.
613
614
615
616

-Bruker Confidential-